arXiv:2504.01651v2 [gr-qc] 6 Aug 2025

Nonlinear electrodynamic black holes and their role in testing modified theories of gravity

Javokhir Sharipov[a], Mirzabek Alloqulov[b,c], Pankaj Sheoran[d], Sanjar Shaymatov[e,f]

[a]*Institute of Fundamental and Applied Research, National Research University TIIAME, Kori Niyoziy 39, 100000, Uzbekistan*
[b]*School of Physics, Harbin Institute of Technology, Harbin, 150001, People's Republic of China*
[c]*University of Tashkent for Applied Sciences, Str. Gavhar 1, Tashkent, 100149, Uzbekistan*
[d]*School of Advanced Sciences, Vellore Institute of Technology, Tiruvalam Rd, Katpadi, Vellore, 632014, Tamil Nadu, India*
[e]*New Uzbekistan University, Movarounnahr Str. 1, Tashkent, 100000, Uzbekistan*
[f]*Institute for Theoretical Physics and Cosmology, Zhejiang University of Technology, Hangzhou, 310023, People's Republic of China*

Abstract

The nature of black holes (BHs) and their potential deviations from classical General Relativity (GR) remain fundamental questions in modern astrophysics. Nonlinear electrodynamics (NED) has been proposed as a viable mechanism to construct regular BHs that avoid singularities while preserving essential astrophysical properties. In this work, we perform a comprehensive analysis of NED-inspired BHs, deriving constraints on the magnetic parameter through Bayesian parameter estimation of the Event Horizon Telescope (EHT) observations, obtaining $q = 0.63^{+0.68}_{-0.44} \times 10^9 M_\odot$ for M87*, and $q = 0.33^{+0.36}_{-0.23} \times 10^6 M_\odot$ for Sgr A*, which influences their horizon structure. A direct comparison with the Schwarzschild BH reveals key deviations in spacetime geometry and horizon properties, reinforcing the role of NED in modifying BH physics. Additionally, we perform a comparative analysis of the observational signatures of these BHs, particularly in the context of BH shadows (using $R_{\rm sh} = r_{\rm ph}\sqrt{1/f(r_{\rm ph})}$, where r_{ph} refers to the radius of the photon sphere) and gravitational lensing, to assess deviations from standard GR solutions. We conduct a detailed analysis of the BH shadow under uniform and non-uniform plasma conditions, demonstrating how deviations from standard GR solutions emerge due to nonlinear electrodynamics. By analyzing deviations in the photon sphere and lensing patterns, we identify key characteristics that distinguish these BHs from standard Schwarzschild BHs. Our findings demonstrate that NED-induced modifications could leave detectable imprints on strong-field astrophysical processes, providing new opportunities to test alternative theories of gravity. Hence, future missions, including the Laser Interferometer Space Antenna (LISA) and next-generation X-ray observatories, will play a crucial role in refining constraints on these theoretical models, building upon our Markov Chain Monte Carlo (MCMC) -constrained parameter space, while complementing ongoing observations from the EHT and gravitational wave detections by LIGO-Virgo, providing a more comprehensive understanding of BH physics and potential deviations from GR.

Keywords: Black hole physics, Gravitational Lensing, Modified Gravity, Plasma, Parameter Estimation

1. Introduction

The study of black holes (BHs), one of the most fascinating predictions of Einstein's General Relativity (GR), has undergone a revolutionary transformation in recent decades, transitioning from theoretical speculation to observational reality. This shift has been driven by groundbreaking advancements in astronomical instrumentation and data analysis. The EHT, a global network of radio telescopes, achieved a historic milestone in 2019 by capturing the first image of a BH's shadow, specifically the supermassive BH at the center of the galaxy M87 Akiyama et al. (2019). This image provided direct visual confirmation of BHs and validated the predictions of GR in the strong-field regime. Around the same time, the Laser Interferometer Gravitational-Wave Observatory (LIGO) made its first detection of gravitational waves in 2015, originating from the merger of two BHs Abbott et al. (2016). These observations have not only confirmed the existence of BHs but also opened new avenues for testing the limits of GR and exploring potential modifications to our understanding of gravity Will (2014); Psaltis et al. (2020).

Despite the remarkable success of GR, several unresolved questions persist, particularly concerning the nature of singularities and the accelerated expansion of the universe. The singularities predicted by GR at the centers of BHs are widely regarded as unphysical, indicating a breakdown of the theory in extreme regimes Hawking and Penrose (1970). Furthermore, the accelerated expansion of the universe, attributed to dark energy, cannot be fully explained within the framework of classical GR Riess et al. (1998); Perlmutter et al. (1999). These limitations have spurred significant interest in alternative gravitational theories, such as those incorporating nonlinear electrodynamics (NED), which can resolve singularities and provide a more complete description of spacetime in the vicinity of BHs Ayon-Beato and Garcia (2000); Bronnikov (2001). NED introduces nonlinear interactions between electromagnetic fields, which can modify the geometry of spacetime near the center of BHs, leading to the formation of regular BHs that lack singularities and instead have a smooth, de-Sitter-like core at their centers Bardeen (1968); Dymnikova (1992), while simultaneously maintaining consistency with key energy conditions Balart and Vagenas (2014); Kumar et al. (2020).

The theoretical foundations of regular BHs trace back to Bardeen's pioneering work Bardeen (1968), with subsequent developments demonstrating how NED couplings can produce singularity-free solutions Ayon-Beato and Garcia (1998); Bronnikov (2001). Modern formulations have established complete families of NED-inspired BH solutions that maintain asymptotic flatness while eliminating central singularities Fan and Wang (2016); Toshmatov et al. (2014); Neves and Saa (2014); Narzilloev et al. (2020), with rotating generalizations being developed more recently Ghosh and Walia (2021). These models not only resolve theoretical pathologies but also predict novel observational signatures through modified photon geodesics and horizon structures Perlick et al. (2018); Abdujabbarov et al. (2016). Recent studies have particularly highlighted how NED parameters influence BH shadows Atamurotov et al. (2021); Kumar et al. (2020); Jafarzade et al. (2025), gravitational lensing characteristics Bisnovatyi-Kogan and Tsupko (2017); Rogers (2015a), and energy extraction processes Penrose (1969); Parthasarathy et al. (1986); Shaymatov et al. (2022); Xamidov et al. (2025), providing multiple avenues for observational testing Shaymatov et al. (2023); Xamidov et al. (2024); Rayimbaev et al. (2022).

In parallel with these theoretical advances, the astrophysical relevance of NED BHs continues to grow through detailed investigations of their observable properties. The shadow morphology

*Corresponding author: Pankaj Sheoran

Email addresses: javohirsh100@gmail.com (Javokhir Sharipov), malloqulov@gmail.com (Mirzabek Alloqulov), pankaj.sheoran@vit.ac.in (Pankaj Sheoran), sanjar@astrin.uz (Sanjar Shaymatov)

of NED BHs exhibits distinct deviations from classical Schwarzschild/Kerr predictions Hioki and Maeda (2009); Cunha et al. (2017), while their lensing signatures show characteristic dependencies on both NED parameters and environmental factors like plasma distributions Er and Mao (2014); Bisnovatyi-Kogan and Tsupko (2010). Furthermore, the thermodynamic behavior of these objects reveals intriguing phase structure analogies with condensed matter systems Kubiznak and Mann (2012); Hendi et al. (2017), suggesting deep connections between quantum gravity and statistical physics.

This work presents a comprehensive investigation of a magnetically charged regular black hole (MCBH) solution within NED, systematically exploring three key observational signatures: (i) shadow properties modified by plasma environments, (ii) gravitational lensing characteristics, and (iii) parameter estimation using EHT data. Building on the framework of Ayon-Beato and Garcia (2000); Balart and Vagenas (2014), we develop a complete phenomenological model that connects theoretical predictions with current observational constraints from the EHT Akiyama et al. (2019); Collaboration (2022). Our analysis of shadow morphology incorporates both analytical and numerical approaches, solving the photon orbit equation $\frac{df}{dr} - \frac{2}{r}f(r) = 0$ to determine the critical impact parameters for both M87* and SgrA* Mustafa et al. (2022). The shadow size $R_{\rm sh} = r_{\rm ph}\sqrt{1/f(r_{\rm ph})}$ is then compared against EHT observations through a rigorous Bayesian framework using the Markov Chain Monte Carlo (MCMC) sampler, yielding precise estimates: $M_{\rm MCBH} = (6.70^{+0.19}_{-0.19}) \times 10^9 M_\odot$ and $q_{\rm MCBH} = 0.63^{+0.68}_{-0.44} \times 10^9 M_\odot$ for M87*, and $M_{\rm MCBH} = (4.08^{+0.19}_{-0.19}) \times 10^6\ M_\odot$ with $q_{\rm MCBH} = 0.33^{+0.36}_{-0.23} \times 10^6 M_\odot$ for Sgr A*. The comparatively lower magnetic charge in SgrA* may indicate weaker NED effects in our Galactic Center, potentially attributable to its relatively quiescent accretion state Genzel et al. (2010); Eckart et al. (2017).

The paper is organized to progressively build our understanding of this NED BH solution. Section 2 establishes the spacetime metric and derives modified photon propagation equations in cold, non-magnetized plasma environments, generalizing the Synge formalism Synge (1966) for both supermassive BH cases, and further analyzes the shadow properties at 230 GHz (M87*) and 345 GHz (Sgr A*), incorporating plasma distributions through the frequency-dependent refractive index $n(\omega)$. Section 3 examines gravitational lensing effects, computing deflection angles using the strong-field expansion technique Bozza et al. (2001) adapted for each source's distance ($D_{\rm M87*} = 16.8$ Mpc, $D_{\rm Sgr\,A*} = 8.3$ kpc). Section 4 quantifies image magnification ratios, comparing the secondary-to-primary flux ratio $\mu_{\rm rel}$ between both systems. Section 5 presents our MCMC framework with likelihood $\log\mathcal{L} = -\frac{1}{2}\sum_i(\theta_{\rm pred} - \theta_{\rm obs})^2/\sigma_i^2$ and distinct priors for each target ($5.5 \times 10^9 M_\odot < M_{M87*} < 7.5 \times 10^9 M_\odot$, $0 \le q_{M87*} < 3.0 \times 10^9 M_\odot$ vs $3.0 \times 10^6 M_\odot < M_{SgrA*} < 6.0 \times 10^6 M_\odot$, $0 < q_{SgrA*} < 2.0 \times 10^6 M_\odot$). Section 6 discusses the implications of our dual-system analysis for testing modified gravity, particularly how Sgr A*'s ∼50% smaller angular shadow diameter constrains NED parameters differently than M87*. Throughout, we employ geometrized units ($G = c = 1$) and the $(-,+,+,+)$ metric signature, with numerical computations performed using the `emcee` package Foreman-Mackey et al. (2013) and `Astropy` for astronomical computations Astropy Collaboration (2013, 2018).

2. Spacetime metric and plasma impact on black hole shadow

In this section, we investigate the dynamics of the photon motion to analyze the shadow of MCBH surrounded by plasma. One can write the static and spherically symmetric BH spacetime

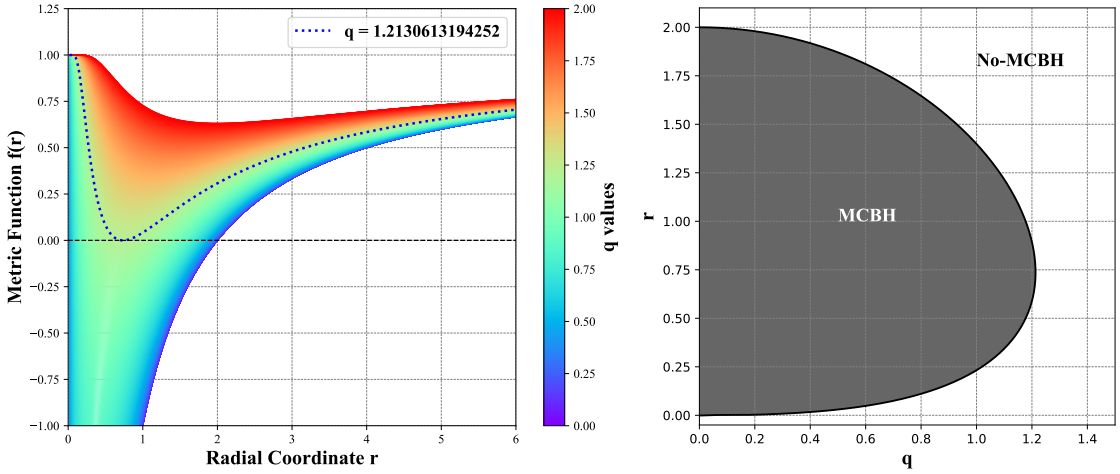

Figure 1: *Left Panel:* The plot illustrates the variation of the function $f(r)$ with respect to the radial coordinate r for different values of the magnetic parameter q. The blue dotted curve represents the extremal case. *Right Panel:* Phase diagram showing the existence of a Magnetically Charged Black Hole (MCBH) region in the (q, r) plane. The black-shaded region represents the parameter space where $f(r, q) \leq 0$, indicating the presence of an MCBH. The boundary line corresponds to the contour $f(r, q) = 0$, separating the MCBH and No-MCBH regions. Here, the mass parameter is set to unity.

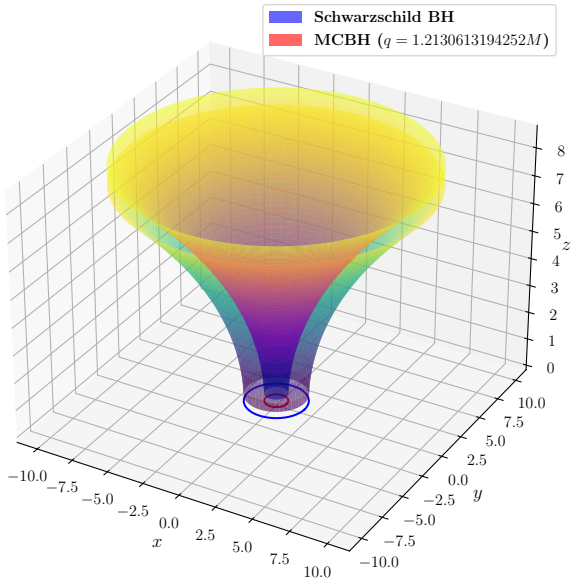

Figure 2: Spatial embedding diagram of a constant-time equatorial slice ($\theta = \pi/2$) of the BH spacetime described by Eq. (1). The surface is embedded into 3D Euclidean space to visualize spatial curvature. The blue surface corresponds to a Schwarzschild BH ($q = 0$), and the magenta surface corresponds to an extremal MCBH with charge parameter $q/M = 1.2130613194252$. Circular rings near the throats indicate the locations of the event horizons: Schwarzschild horizon at $r/M = 2$ (blue)and extremal MCBH horizon at $r_{\text{horizon}}/M = 0.735759$ (red).

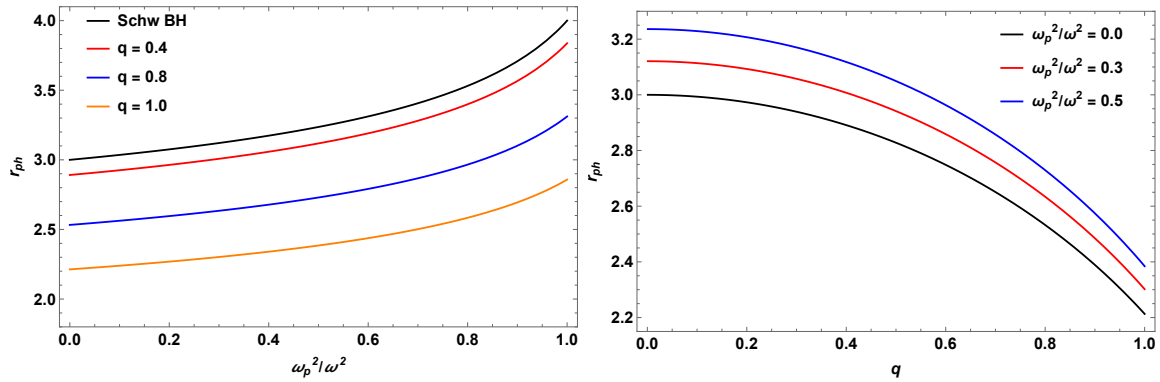

Figure 3: Left panel: The photon sphere radius as a function of plasma frequency for different values of the magnetic charge. Right panel: The dependence of the radius of the photon sphere on the magnetic charge q for different values of the plasma frequency.

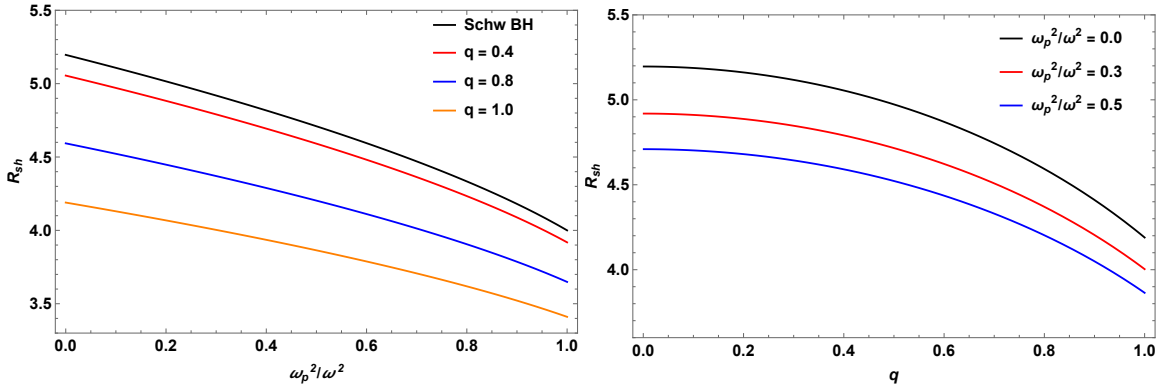

Figure 4: Left panel: The shadow radius as a function of plasma frequency for different values of the magnetic charge. Right panel: The dependence of the radius of the shadow on the magnetic charge q for different values of the plasma frequency.

in Boyer-Lindquist coordinates in the following form Ali et al. (2020)

$$ds^2 = -f(r)dt^2 + \frac{dr^2}{f(r)} + r^2(d\theta^2 + \sin^2\theta d\phi^2)\,, \tag{1}$$

In this work, we consider GR coupled to a NED field. We adopt an effective Lagrangian of the form Ali et al. (2020)

$$\mathcal{L}_{\rm NED} = Fe^{-\frac{q}{2M}(2q^2F)^{1/4}}\,, \tag{2}$$

where q is the magnetic charge parameter, and $F = \frac{1}{4}F_{\mu\nu}F^{\mu\nu}$ is the electromagnetic field invariant, with $F_{\mu\nu} = \partial_\mu A_\nu - \partial_\nu A_\mu$.

We note that this Lagrangian depends explicitly on the parameters M and q of the particular BH solution it supports. Therefore, it should be interpreted as a phenomenological or solution-generating ansatz rather than a fundamental Lagrangian for NED. Such constructions have been

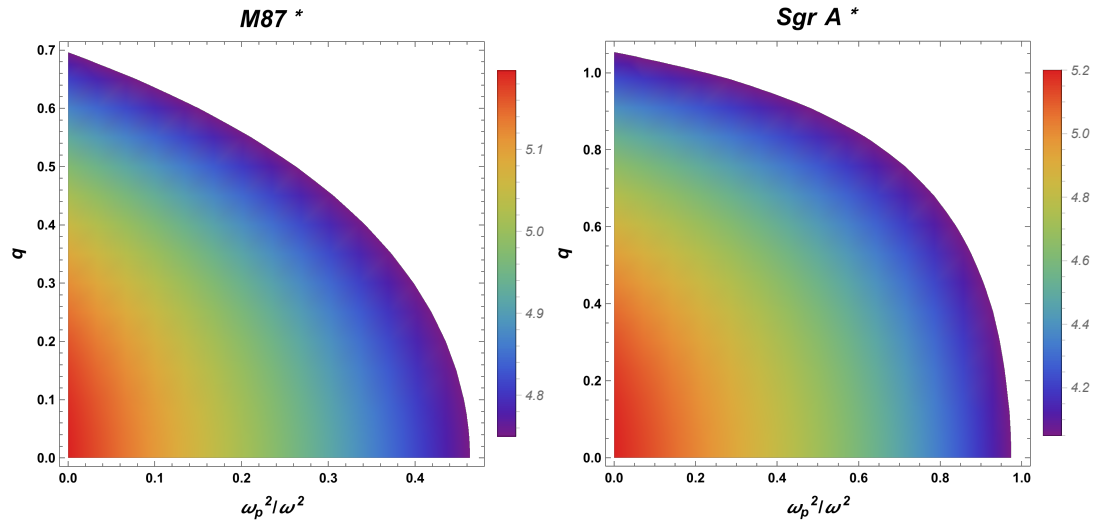

Figure 5: The constrained values of the magnetic charge parameter q and ω_p^2/ω^2 for supermassive BHs sitting at the center M87* and Sgr A* galaxies.

employed in the literature to obtain regular or modified BH solutions with desired properties (e.g., Ali et al. (2020)). Nonetheless, the lack of universality in the Lagrangian makes its interpretation as a fundamental theory of electromagnetism problematic, especially in the $M \to 0$ limit. Our objective here is not to develop a complete theory of NED, but rather to explore the consequences of such a solution on photon motion and BH shadow.

For the static, spherically symmetric magnetic BH solution, we choose the NED invariant to take the form $F = \frac{q^2}{2r^4}$, which yields the effective Lagrangian

$$\mathcal{L}_{\rm NED} = \frac{q^2}{2r^4} e^{-\frac{q^2}{2Mr}} \,. \tag{3}$$

Using this Lagrangian, the non-zero components of the energy-momentum tensor are given by

$$T_0^0 = T_1^1 = -\frac{q^2}{r^4} e^{-\frac{q^2}{2Mr}} \,, \tag{4}$$

$$T_2^2 = T_3^3 = \frac{q^2}{4Mr^5}(q^2 - 4Mr) e^{-\frac{q^2}{2Mr}} \,. \tag{5}$$

To determine the spacetime geometry, we solve the Einstein field equations

$$G_{\mu\nu} = R_{\mu\nu} - \frac{1}{2} R g_{\mu\nu} = T_{\mu\nu} \,, \tag{6}$$

for a static, spherically symmetric metric. The relevant component of the Einstein tensor is

$$G_0^0 = G_1^1 = -\frac{1}{r}\frac{df(r)}{dr} - \frac{f(r)}{r^2} + \frac{1}{r^2} \,. \tag{7}$$

Solving Eq. (6) with the energy-momentum components in Eqs. (4) and (7), we obtain the metric function as

$$f(r) = 1 - \frac{2M}{r} e^{-\frac{q^2}{2Mr}}, \tag{8}$$

where q denotes the magnetic charge of the black hole. In the limit $q \to 0$, the solution reduces to the Schwarzschild spacetime, as expected.

To better understand the geometric features of this magnetic charged black hole (MCBH), we study the behavior of the metric function $f(r)$ and determine the parameter ranges for which the solution describes a black hole. For convenience in the subsequent analysis, we normalize the radial coordinate and magnetic charge as $r \to r/M$ and $q \to q/M$.

To determine the extremal configuration of the MCBH spacetime, we analytically solve the conditions for extremality, which require the degenerate horizon to satisfy

$$f(r) = 0 \quad \text{and} \quad f'(r) = 0. \tag{9}$$

We impose the condition $f(r) = 0$, which gives

$$\frac{2M}{r} e^{-q^2/2Mr} = 1. \tag{10}$$

Taking the natural logarithm of both sides, we find

$$\ln\left(\frac{2M}{r}\right) = \frac{q^2}{2Mr}. \tag{11}$$

Now, differentiating $f(r)$ with respect to r, we get

$$f'(r) = \frac{2M}{r^2} e^{-q^2/2Mr} \left(1 - \frac{q^2}{2Mr}\right). \tag{12}$$

Setting $f'(r) = 0$, we obtain the second condition:

$$1 - \frac{q^2}{2Mr} = 0 \quad \Rightarrow \quad r = \frac{q^2}{2M}. \tag{13}$$

Substituting this value of r back into the earlier logarithmic equation, we find:

$$\ln\left(\frac{2M}{r}\right) = \frac{q^2}{2Mr} = 1, \tag{14}$$

which implies

$$\frac{2M}{r} = e \quad \Rightarrow \quad r = \frac{2M}{e}. \tag{15}$$

Using this value in $r = \frac{q^2}{2M}$, we obtain

$$\frac{2M}{e} = \frac{q^2}{2M} \quad \Rightarrow \quad q_{\text{ext}} = \frac{2M}{\sqrt{e}}. \tag{16}$$

Hence, the extremal magnetic charge is given by $q_{\text{ext}}/M = 2/\sqrt{e} \approx 1.21306$, and the correspond-

ing extremal horizon radius is $r_{\rm ext}/M = 2/e \approx 0.73576$.

The left panel of Fig. 1 shows the variation of $f(r)$ with respect to the radial coordinate r for different values of the magnetic charge parameter q. The function $f(r)$ determines the location of the event horizon, which is obtained by solving $f(r) = 0$. The blue-dotted curve represents the extremal case where the two horizons coincide, leading to a single degenerate root. For larger values of q, the horizon structure is significantly altered, indicating a strong dependence of the BH's causal structure on the magnetic charge. The right panel of Fig. 1 presents the phase diagram in the (q, r) parameter space, showing the regions where an MCBH solution exists. The black-shaded region represents the domain where $f(r, q) \leq 0$, corresponding to the presence of a BH, while the white region corresponds to no MCBH (No-MCBH). The boundary between these regions is given by the contour $f(r, q) = 0$, which separates the MCBH and No-MCBH regimes.

To further visualize the impact of the magnetic charge on the spatial geometry of the BH exterior, we construct an embedding diagram of a constant-time, equatorial ($\theta = \pi/2$) slice of the spacetime. The induced 2-dimensional spatial metric in this slice is given by

$$ds^2 = \frac{dr^2}{f(r)} + r^2 d\phi^2, \tag{17}$$

which can be embedded as a surface of revolution $z = z(r)$ in 3-dimensional Euclidean space, with the line element

$$ds^2 = \left[1 + \left(\frac{dz}{dr}\right)^2\right] dr^2 + r^2 d\phi^2. \tag{18}$$

By matching the two expressions, we obtain the differential equation

$$\left(\frac{dz}{dr}\right)^2 = \frac{1}{f(r)} - 1, \tag{19}$$

which we solve numerically to generate the embedded surfaces. The resulting geometry provides an intuitive visualization of how the spatial curvature is influenced by the BH. Figure 2 shows the embedded diagrams for both a Schwarzschild BH ($q = 0$) and an extremal MCBH with charge parameter $q/M = \frac{2}{\sqrt{e}} \approx 1.21306$. The Schwarzschild horizon, located at $r/M = 2$, is shown in blue, while the extremal MCBH horizon is depicted in red at $r_{\rm horizon}/M = \frac{2}{e} \approx 0.73576$, where e is Euler's number. This comparison clearly demonstrates how increasing the magnetic charge q reduces the horizon radius and significantly alters the spatial geometry, culminating in an extremal configuration with a minimal horizon size.

To explore the motion of photons around an MCBH, we employ the Hamilton-Jacobi equation. The Hamiltonian for null geodesics around an MCBH in plasma is given as follows Synge (1960):

$$\mathcal{H}(x^\alpha, p_\alpha) = \frac{1}{2}\left[g^{\alpha\beta} p_\alpha p_\beta - (n^2 - 1)(p_\beta u^\beta)^2\right], \tag{20}$$

where x^α refers to the spacetime coordinates, u^β and p_α are the four-velocity and four-momentum of the photon, respectively. It is worth noting that in the above equation, n is the refractive index which can be determined as $n = \omega/k$ where k is the wave number. It can be written as Tsupko

and Bisnovatyi-Kogan (2009)

$$n^2 = 1 - \frac{\omega_{\rm p}^2}{\omega^2}\,, \tag{21}$$

where $\omega_p^2(x^\alpha) = 4\pi e^2 N(x^\alpha)/m_e$ is the plasma frequency, and e and m_e refer to the electron mass and charge, respectively. N is the number density of the electrons. Using the $\omega^2 = (p_\beta u^\beta)^2$, one can define the photon frequency as

$$\omega(r) = \frac{\omega_0}{\sqrt{f(r)}}\,, \qquad \omega_0 = \text{const}\,. \tag{22}$$

with $f(r) \to 1$ is satisfied as $r \to \infty$ and $\omega(\infty) = \omega_0 = -p_t$ Perlick et al. (2015). Here, we adopt a simplified model in which the plasma is assumed to be non-magnetized, isotropic, and pressureless, and the interaction with the BH is purely gravitational. This assumption follows the standard treatment used in earlier works on Schwarzschild BHs Perlick et al. (2015). However, for magnetically charged BHs, an additional Lorentz force may arise due to electromagnetic coupling with the plasma. Such effects could potentially alter the plasma distribution and influence photon trajectories, but a consistent treatment would require a more detailed magnetohydrodynamic (MHD) analysis, which we leave for future work.

Now, to describe photon trajectories in a plasma environment around the BH, we adopt a Hamiltonian formalism. Specifically, the Hamiltonian for photons propagating through a non-magnetized, pressureless plasma takes the form Synge (1960); Rogers (2015b)

$$\mathcal{H} = \frac{1}{2}\left[g^{\alpha\beta}p_\alpha p_\beta + \omega_{\rm p}^2\right]. \tag{23}$$

Instead of using the Hamilton-Jacobi equation, we derive the equations of motion for photons by employing Hamilton's equations:

$$\dot{x}^\mu = \frac{\partial \mathcal{H}}{\partial p_\mu}, \qquad \dot{p}_\mu = -\frac{\partial \mathcal{H}}{\partial x^\mu}. \tag{24}$$

This approach directly yields the following geodesic equations in the equatorial plane ($\theta = \pi/2$):

$$\dot{t} \equiv \frac{dt}{d\lambda} = \frac{-p_t}{f(r)}, \tag{25}$$

$$\dot{r} \equiv \frac{dr}{d\lambda} = p_r f(r), \tag{26}$$

$$\dot{\phi} \equiv \frac{d\phi}{d\lambda} = \frac{p_\phi}{r^2}, \tag{27}$$

where λ is an affine parameter along the null geodesic. The system is then numerically integrated using initial conditions based on conserved quantities p_t and p_ϕ.

We can use Eqs. (26) and (27) to obtain the orbit equation as

$$\frac{dr}{d\phi} = \frac{g^{rr}p_r}{g^{\phi\phi}p_\phi}\,. \tag{28}$$

For the light geodesics $\mathcal{H} = 0$, one can rewrite the above equation as

$$\frac{dr}{d\phi} = \sqrt{\frac{g^{rr}}{g^{\phi\phi}}}\sqrt{\gamma^2(r)\frac{\omega_0^2}{p_\phi^2} - 1}\,, \tag{29}$$

where the following relationship holds true

$$\gamma^2(r) \equiv -\frac{g^{tt}}{g^{\phi\phi}} - \frac{\omega_p^2}{g^{\phi\phi}\omega_0^2}\,. \tag{30}$$

We can obtain the radius of the photon sphere from the following equation

$$\frac{d(\gamma^2(r))}{dr} = \frac{d^2(\gamma^2(r))}{dr^2}\bigg|_{r=r_{\rm ph}} = 0\,. \tag{31}$$

Using the above equation, we explore the radius of the photon sphere numerically and we demonstrate the dependence of the radius of the photon sphere on magnetic parameter q and plasma frequency in Fig. 3. One can observe from this figure that the radius of the photon sphere increases with the increase of the frequency of the plasma, while it decreases under the influence of the magnetic parameter.

One can determine the boundary of the shadow α_{sh} through the light rays that spiral asymptotically towards a circular light orbit at radius r_{ph}. In the next subsection, we investigate the BH shadow in plasma.

Black hole shadow in plasma: In this subsection, we study the shadow of the magnetically charged BH in the presence of plasma. One can obtain the angular radius α_{sh} of the BH as follows Perlick et al. (2015); Konoplya (2019)

$$\begin{aligned}\sin^2\alpha_{\rm sh} &= \frac{\gamma^2(r_{\rm ph})}{\gamma^2(r_{\rm o})},\\ &= \frac{r_{\rm ph}^2\left[\frac{1}{f(r_{\rm ph})} - \frac{\omega_p^2(r_{\rm ph})}{\omega_0^2}\right]}{r_{\rm o}^2\left[\frac{1}{f(r_{\rm o})} - \frac{\omega_p^2(r_{\rm o})}{\omega_0^2}\right]},\end{aligned} \tag{32}$$

where r_o and r_{ph} refer to the locations of the observer and the photon sphere, respectively. If the observer is positioned at a distance far enough from the BH the radius of the BH shadow can be approximated using the above equation as Konoplya (2019)

$$\begin{aligned}R_{\rm sh} &\simeq r_{\rm o}\sin\alpha_{\rm sh},\\ &= \sqrt{r_{\rm ph}^2\left[\frac{1}{f(r_{\rm ph})} - \frac{\omega_p^2(r_{\rm ph})}{\omega_0^2}\right]},\end{aligned} \tag{33}$$

Here, we have utilized the fact that $\gamma(r_{\rm o}) \to r_{\rm o}$ approaches spatial infinity, a result derived from Eq. (30) by considering the observer is located far distance and the assumption that the density of the plasma is negligible in this region. However, plasma can affect the values of the BH shadow. Fig. 4 shows the dependence of the BH shadow on the magnetic parameter q and

plasma frequency. It can be seen from this figure that the radius of the BH shadow decreases with the increase of the magnetic parameter q. Also, there is a decrease under the influence of the plasma frequency. Additionally, we assume that the compact objects M87* and Sgr A* are static and spherically symmetric, despite observations from the EHT collaboration that do not support this assumption. We theoretically explore the limits of the magnetic parameter q of MCBH, using the data provided by the EHT collaboration. We chose the BH's magnetic parameter q and the plasma frequency for constraint. According to the data provided by the EHT collaboration, the angular diameter θ_{M87*} of the BH shadow, the distance from Earth and the mass of the BH at the center of the M87* are $\theta_{M87*} = 42 \pm 3\mu as$, $D = 16.8 \pm 0.8Mpc$ and $M_{M87*} = 6.5 \pm 0.7 \times 10^9 M_\odot$ Akiyama and et al. (Event Horizon Telescope Collaboration) (2019a), respectively. For Sgr A*, the data provided by the EHT collaboration are $\theta_{SgrA*} = 48.7 \pm 7\mu as$, $D = 8277 \pm 9 \pm 33pc$ and $M_{SgrA*} = 4.297 \pm 0.013 \times 10^6 M_\odot$ (VLTI) Akiyama and et al. (Event Horizon Telescope Collaboration) (2021). Using the above information, one can calculate the diameter of the shadow caused by the compact object per unit mass in the following form Bambi et al. (2019)

$$d_{sh} = \frac{D\theta}{M} \tag{34}$$

From the expression $d_{sh} = 2R_{sh}$, one can easily obtain the expression for the diameter of the BH shadow. Here, the distance D is considered a dimension of mass M Akiyama and et al. (Event Horizon Telescope Collaboration) (2019a,b). Hence, the diameter of the BH shadow $d_{sh}^{M87*} = (11 \pm 1.5)M$ for M87* and $d_{sh}^{Sgr*} = (9.5 \pm 1.4)M$ for Sgr A*. Finally, the limits of the magnetic parameter q of the BH and the plasma frequency for the supermassive BHs at the centers of the galaxies M87* and Sgr A* can be obtained. Using the "color map", we demonstrate the limits of the magnetic parameter q and the plasma frequency ω_p^2/ω^2 in Fig. 5.

3. Gravitational weak lensing for MCBH

In this section, the weak gravitational lensing was investigated under two different plasma distributions, which are uniform and non-uniform plasma. It is common to express the spacetime metric as a slight deviation from the flat spacetime as Bisnovatyi-Kogan and Tsupko (2010, 2009); Babar et al. (2021)

$$g_{\alpha\beta} \approx \eta_{\alpha\beta} + h_{\alpha\beta} \,, \tag{35}$$

where $\eta_{\alpha\beta}$ and $h_{\alpha\beta}$ refer to the Minkowski spacetime and small perturbation gravity field, respectively. One can write the following conditions for them

$$\begin{aligned} &\eta_{\alpha\beta} = diag(-1, 1, 1, 1) \,, \\ &h_{\alpha\beta} \ll 1, \quad h_{\alpha\beta} \to 0 \quad under \;\; x^\alpha \to \infty \,, \\ &g^{\alpha\beta} = \eta^{\alpha\beta} - h^{\alpha\beta}, \quad h^{\alpha\beta} = h_{\alpha\beta} \,. \end{aligned} \tag{36}$$

One can write the following equation for the deflection angle around MCBH as Bisnovatyi-Kogan and Tsupko (2017, 2009)

$$\hat{\alpha}_{\rm b} = \int \frac{b}{2r}\left(\frac{dh_{33}}{dr} + \frac{1}{1-\frac{\omega_p^2}{\omega^2}}\frac{dh_{00}}{dr} - \frac{K_e}{\omega^2-\omega_p^2}\frac{dN}{dr}\right)dz \,, \tag{37}$$

where ω and ω_p refer to the photon and plasma frequencies, respectively, and and $K_e = 4\pi e^2/m_e$. The result of expanding the metric functions in a Taylor series is written as follows:

$$\begin{aligned} g_{tt} &= -f(r) \approx -1 + \frac{2M}{r} - \frac{q^2}{r^2} + \frac{q^4}{4Mr^3}\,, \\ g_{rr} &= \frac{1}{f(r)} \approx 1 + \frac{2M}{r} + \frac{4M^2 - q^2}{r^2} + \left(8M^3 - 4Mq^2 + \frac{q^4}{4M}\right)\frac{1}{r^3}\,. \end{aligned} \tag{38}$$

It is worth noting that we can recover the RN BH in the second-order approximation. However, next-order terms play an important role in analyzing the effects of the NED on the gravitational weak lensing, together with the effect of magnetic charge q. The higher order term, $\frac{q^4}{4Mr^3}$, reveals the modification. Using Eq. (38), we write the line element as

$$\begin{aligned} ds^2 &= ds_0^2 + \left(\frac{2M}{r} - \frac{q^2}{r^2} + \frac{q^4}{4Mr^3}\right)dt^2 \\ &\quad + \left(\frac{2M}{r} + \frac{4M^2 - q^2}{r^2} + \frac{8M^3}{r^3} - \frac{4Mq^2}{r^3} + \frac{q^4}{4Mr^3}\right)dr^2\,, \end{aligned} \tag{39}$$

with $ds_0^2 = -dt^2 + dr^2 + r^2(d\theta^2 + \sin^2\theta d\phi^2)$. Furthermore, the components of the metric perturbations $h_{\alpha\beta}$ can be obtained as

$$h_{00} = \frac{2M}{r} - \frac{q^2}{r^2} + \frac{q^4}{4Mr^3}\,, \tag{40}$$

$$h_{ik} = \left(\frac{2M}{r} + \frac{4M^2 - q^2}{r^2} + \frac{8M^3}{r^3} - \frac{4Mq^2}{r^3} + \frac{q^4}{4Mr^3}\right)n_i n_k\,, \tag{41}$$

$$h_{33} = \left(\frac{2M}{r} + \frac{4M^2 - q^2}{r^2} + \frac{8M^3}{r^3} - \frac{4Mq^2}{r^3} + \frac{q^4}{4Mr^3}\right)\cos^2\chi\,, \tag{42}$$

with $r^2 = b^2 + z^2$ and $\cos^2\chi = z^2/(b^2 + z^2)$, n_i, n_k - components of the unit vector of the radius vector. Here, we use the impact parameter b and the z-axis to describe the spatial position of the photon. χ is the polar angle between the z-axis and the radius vector. The first-order derivatives of h_{00} and h_{33}, taken in terms of the radial coordinate, are written as follows:

$$\frac{dh_{00}}{dr} = -\frac{2M}{r^2} + \frac{2q^2}{r^3} - \frac{3q^4}{4Mr^4}, \tag{43}$$

$$\frac{dh_{33}}{dr} = \left(-\frac{6M}{r^4} + \frac{4q^2}{r^5} - \frac{16M^2}{r^5} - \frac{5q^4}{4Mr^6} + \frac{20Mq^2}{r^6} - \frac{40M^3}{r^6}\right)z^2\,. \tag{44}$$

The equation for the deflection angle can be written as

$$\hat{\alpha_b} = \hat{\alpha_1} + \hat{\alpha_2} + \hat{\alpha_3}\,, \tag{45}$$

with

$$\begin{aligned}
\hat{\alpha_1} &= \frac{1}{2}\int_{-\infty}^{\infty}\frac{b}{r}\frac{dh_{33}}{dr}dz\,,\\
\hat{\alpha_2} &= \frac{1}{2}\int_{-\infty}^{\infty}\frac{b}{r}\frac{1}{1-\omega_p^2/\omega^2}\frac{dh_{00}}{dr}dz\,,\\
\hat{\alpha_3} &= \frac{1}{2}\int_{-\infty}^{\infty}\frac{b}{r}\left(-\frac{K_e}{\omega^2-\omega_p^2}\frac{dN}{dr}\right)dz\,.
\end{aligned} \tag{46}$$

In the following subsections, we consider the effect of uniform and non-uniform plasma distributions on the deflection angle.

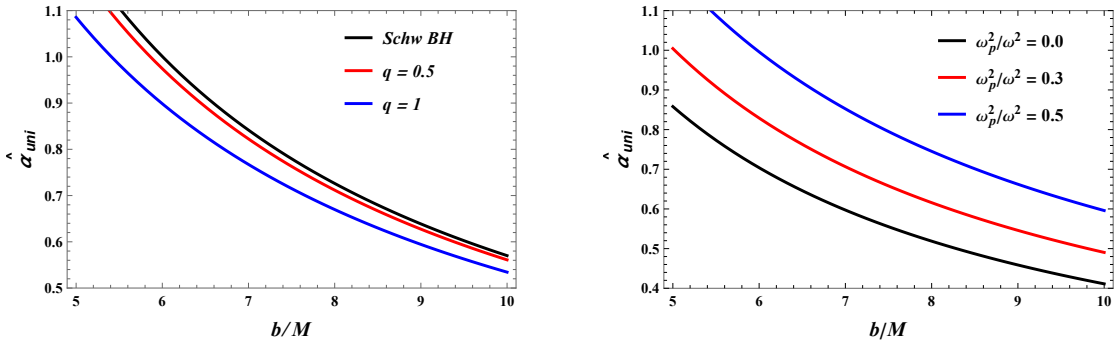

Figure 6: The deflection angle of the light around MCBH $\hat{\alpha}_{\rm uni}$ as a function of the impact parameter b/M for different values of magnetic charge q (left panel) and uniform plasma frequency (right panel).

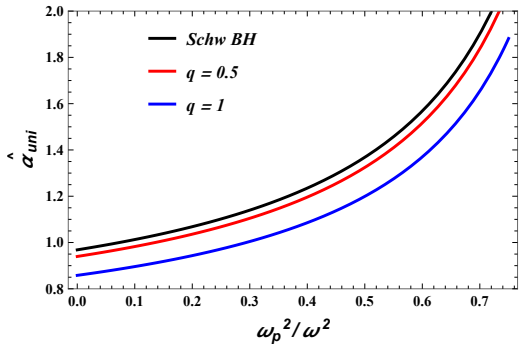

Figure 7: The plot demonstrates the dependence of the deflection angle $\hat{\alpha}_{\rm uni}$ on the uniform plasma frequency for different values of the magnetic charge q. Here, we set $b/M = 5$.

Uniform plasma case: Here, we explore the impact of the uniform plasma on the deflection angle with the assumption that MCBH is surrounded by uniform plasma. Taking into account uniform plasma, we can rewrite Eq. (45) as

$$\hat{\alpha}_{uni} = \hat{\alpha}_{uni1} + \hat{\alpha}_{uni2} + \hat{\alpha}_{uni3}. \tag{47}$$

Using Eq. (46), the defection angle for the MCBH surrounded by uniform plasma can be written in the following form

$$\begin{aligned}\hat{\alpha}_{uni} &= \frac{2M}{b}+\frac{\pi M^2}{b^2}-\frac{\pi q^2}{4b^2}+\frac{16M^3}{3b^3}+\frac{q^4}{6b^3M}\\ &\quad -\frac{8Mq^2}{3b^3}+\left(\frac{2M}{b}-\frac{\pi q^2}{2b^2}+\frac{q^4}{2b^3M}\right)\frac{\omega^2}{\omega^2-\omega_p^2},\end{aligned} \tag{48}$$

Using the above equation, we plot the dependence of the deflection angle on the impact parameter for different values of the magnetic charge q and uniform plasma frequency in Fig. 6. From this figure, one can see that the values of the deflection angle decrease with increasing magnetic charge q. In contrast, there is an increase under the influence of the uniform plasma frequency. To be more informative, we plot the dependence of the deflection angle on the uniform plasma frequency in Fig. 7.

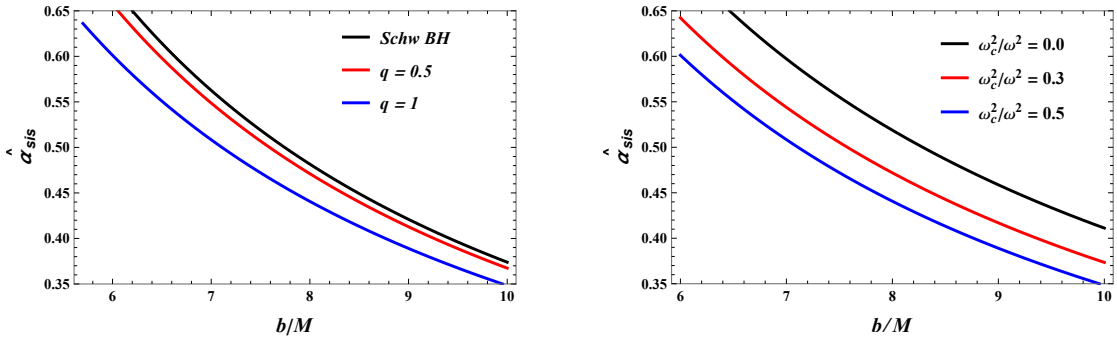

Figure 8: The deflection angle of the light around MCBH $\hat{\alpha}_{\rm sis}$ as a function of the impact parameter b/M for different values of magnetic charge q (left panel) and non-uniform plasma frequency (right panel).

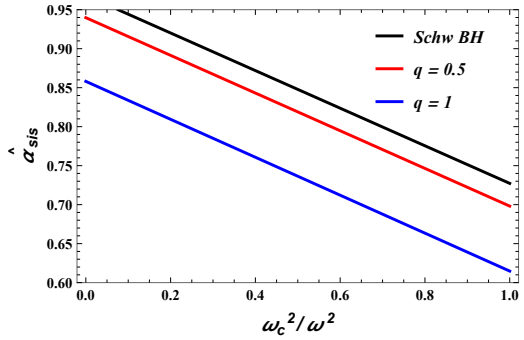

Figure 9: The plot illustrates the dependence of the deflection angle $\hat{\alpha}_{\rm sis}$ on the non-uniform plasma frequency for different values of the magnetic charge q. Here, we set $b/M = 5$.

Non-uniform plasma case: In this part, we consider the singular isothermal sphere (SIS) and analyze its effect on the deflection angle around MCBH. The density distribution of SIS can be

written as Bisnovatyi-Kogan and Tsupko (2010); Bartelmann and Schneider (2001)

$$\rho(r) = \frac{\sigma_v^2}{2\pi r^2} \,, \tag{49}$$

with σ_v^2 refers to an one-dimensional velocity dispertion. One can write the plasma concentration of SIS in the following form Bisnovatyi-Kogan and Tsupko (2009, 2010)

$$N(r) = \frac{\rho(r)}{\kappa \cdot m_p} \,, \tag{50}$$

where κ and m_p refer to a dimensionless constant and the proton mass, respectively. We can define the plasma frequency as Bisnovatyi-Kogan and Tsupko (2010)

$$\omega_c^2 = K_e N(r) = \frac{K_e \sigma_v^2}{2\pi\kappa m_p r^2} \,. \tag{51}$$

To analyze the effects of non-uniform plasma (SIS), it is necessary to express the deflection angle around the BH. It can be written as

$$\hat{\alpha}_{SIS} = \hat{\alpha}_{SIS1} + \hat{\alpha}_{SIS2} + \hat{\alpha}_{SIS3} \,. \tag{52}$$

From Eqs. (42), (46), and (52), we can analytically derive the deflection angle for MCBH surrounded by SIS as

$$\begin{aligned}\hat{\alpha}_{SIS} =& \frac{4M}{b} - \frac{4M^2\omega_c^2}{\pi b\omega^2} + \frac{\pi M^2}{b^2} - \frac{3\pi q^2}{4b^2} + \frac{16M^3\omega_c^2}{3\pi b^3\omega^2} \\ &+ \frac{16M^3}{3b^3} + \frac{2q^4}{3b^3M} - \frac{8Mq^2}{3b^3} - \frac{3M^2q^2\omega_c^2}{2b^4\omega^2} + \frac{8Mq^4\omega_c^2}{5\pi b^5\omega^2} \,.\end{aligned} \tag{53}$$

One can write the explicit form of the plasma frequency as Bisnovatyi-Kogan and Tsupko (2010)

$$\omega_c^2 = \frac{K_e \sigma_v^2}{2\pi\kappa m_p R_S^2} \,, \tag{54}$$

where $R_S = 2M$. In Fig. 8, the dependence of the deflection angle around MCBH surrounded by non-uniform plasma on the impact parameter for different values of the magnetic charge q and plasma frequency was demonstrated. We can see from this figure that there is a decrease under the influence of both the magnetic charge and plasma frequency. Also, the deflection angle decreases as the impact parameter b/M grows. To better understand, we also plot the dependence of the deflection angle on the non-uniform plasma frequency in Fig. 9. In addition, we compare the deflection angles for uniform and non-uniform plasma in Fig. 10. It is seen that the deflection angle for the uniform is higher than the deflection angle for the non-uniform plasma.

4. Magnification of gravitationally lensed image

Now we explore the magnification of the gravitational lensed image around MCBH by using the angle of the deflection. One can write the following equation for the light angles around

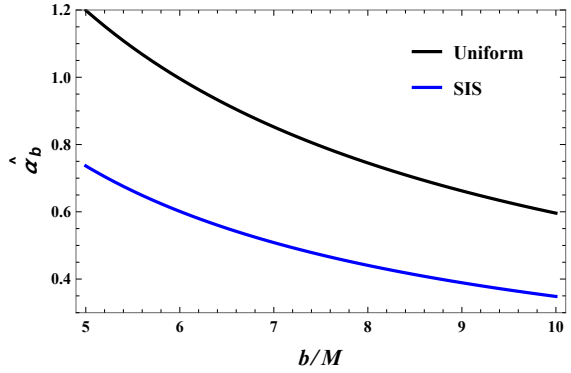

Figure 10: The plot shows a comparison between the deflection angles for uniform and non-uniform plasma.

MCBH $\hat{\alpha}_b$, θ, and β Bozza (2008); Babar et al. (2021); Schneider et al. (1992)

$$\theta D_{\rm s} = \beta D_{\rm s} + \hat{\alpha} D_{\rm ds} \,, \tag{55}$$

where $D_{\rm s}$, $D_{\rm d}$ and $D_{\rm ds}$ are the distances: source-observer, lens-observer, and source-lens, respectively. θ and β refer to the angular position of the image and the angular position of the source, respectively. Using (Eq. 55), we can express the angular position of the source as

$$\beta = \theta - \frac{D_{\rm ds}}{D_{\rm s}} \frac{\xi(\theta)}{D_{\rm d}} \frac{1}{\theta} \,, \tag{56}$$

where $\xi(\theta) = |\hat{\alpha}_b| b$ and $b = D_{\rm d}\theta$. The image can be recognized as Einstein's ring, having a radius $R_s = D_{\rm d}\theta_E$ with the assumption that it appears as a ring. The corresponding angular part θ_E can be expressed as

$$\theta_E = \sqrt{2R_s \frac{D_{ds}}{D_d D_s}} \,. \tag{57}$$

After that, one can write the brightness magnification as

$$\mu_\Sigma = \frac{I_{\rm tot}}{I_*} = \sum_k \left| \left(\frac{\theta_k}{\beta} \right) \left(\frac{d\theta_k}{d\beta} \right) \right|, \quad k = 1, 2, \ldots, j \,, \tag{58}$$

where $I_{\rm tot}$ and I_* are the total and unlensed brightness of the source, respectively. Then the magnification of the source is determined as follows Alloqulov et al. (2023, 2024a,b)

$$\mu_+^{\rm pl} = \frac{1}{4} \left(\frac{x}{\sqrt{x^2+4}} + \frac{\sqrt{x^2+4}}{x} + 2 \right) , \tag{59}$$

$$\mu_-^{\rm pl} = \frac{1}{4} \left(\frac{x}{\sqrt{x^2+4}} + \frac{\sqrt{x^2+4}}{x} - 2 \right) , \tag{60}$$

where $x = \beta/\theta_E$ is the dimensionless parameter. Then we can derive the total magnification as

$$\mu_{\rm tot}^{\rm pl} = \mu_{+}^{\rm pl} + \mu_{-}^{\rm pl} = \frac{x^2+2}{x\sqrt{x^2+4}}\,. \tag{61}$$

In the following subsections, we analyze image magnification of the source using two different plasma distributions which are uniform and non-uniform plasma.

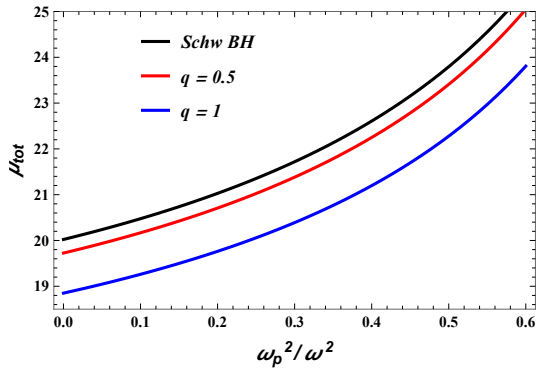

Figure 11: The total magnification μ_{tot} as a function of the uniform plasma frequency ω_P^2/ω^2 for different values of magnetic charge. Here, we set $b/M = 5$.

Uniform plasma case: Here, we investigate the effect of the uniform plasma on the magnification of the lensed image as mentioned above. We can rewrite Eq. (61) considering that MCBH is surrounded by a uniform plasma as

$$\mu_{tot}^{pl} = \mu_{+}^{pl} + \mu_{-}^{pl} = \frac{x_{uni}^2+2}{x_{uni}\sqrt{x_{uni}^2+4}}\,, \tag{62}$$

where x_{uni}, $(\mu_{+}^{pl})_{uni}$ and $(\mu_{-}^{pl})_{uni}$ are specified as follows:

$$\begin{aligned} x_{uni} &= \frac{\beta}{(\theta_E^{pl})_{uni}} \qquad (63)\\ &= \sqrt{2}x_0\left[1+\frac{\pi M}{2b}-\frac{\pi q^2}{8bM}+\frac{8M^2}{3b^2}-\frac{4q^2}{3b^2}+\frac{q^4}{12b^2M^2}+\left(1-\frac{\pi q^2}{4bM}+\frac{q^4}{4b^2M^2}\right)\frac{1}{1-\frac{\omega_P^2}{\omega^2}}\right]^{-1/2}, \end{aligned}$$

$$(\mu_{+}^{pl})_{uni} = \frac{1}{4}\left(\frac{x_{uni}}{\sqrt{x_{uni}^2+4}}+\frac{\sqrt{x_{uni}^2+4}}{x_{uni}}+2\right), \tag{64}$$

$$(\mu_{-}^{pl})_{uni} = \frac{1}{4}\left(\frac{x_{uni}}{\sqrt{x_{uni}^2+4}} + \frac{\sqrt{x_{uni}^2+4}}{x_{uni}} - 2\right). \tag{65}$$

Fig. 11 shows the dependence of the total magnification on the frequency of the uniform plasma for different values of the magnetic charge parameter q. We can see from this figure that there is a slight decrease under the influence of the magnetic charge parameter.

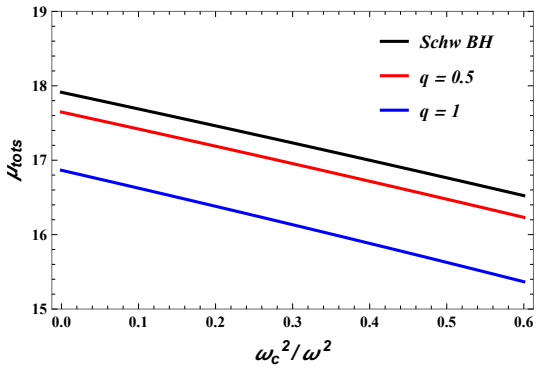

Figure 12: The total magnification μ_{tots} as a function of the non-uniform plasma frequency ω_c^2/ω^2 for different values of magnetic charge. Here, we set $b/M = 5$.

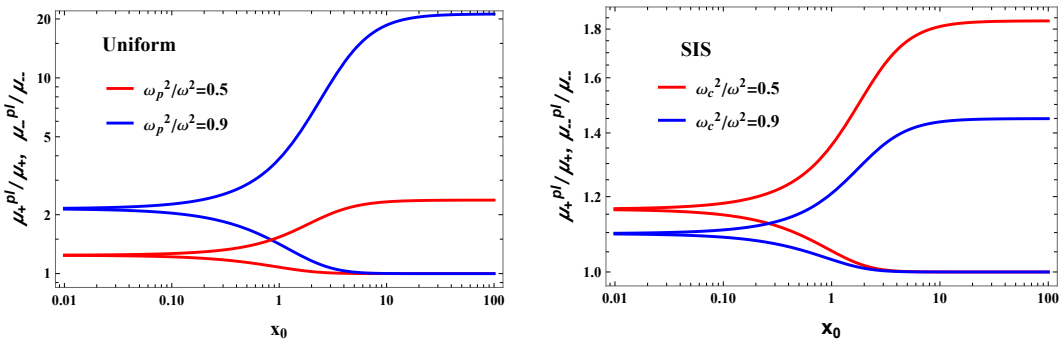

Figure 13: The plot demonstrates the image magnification as a function of x_0. The left/right panel corresponds to the uniform/SIS plasma. Here, we set $b/M = 3$ and q/M=1.

Non-uniform plasma case: Now we consider the non-uniform plasma (SIS model) and analyze its effect on magnification. By rewriting the Eq. (61) for the non-uniform plasma, we can find the total magnification as Schneider et al. (1992)

$$(\mu_{tot}^{pl})_{SIS} = (\mu_{+}^{pl})_{SIS} + (\mu_{-}^{pl})_{SIS} = \frac{x_{SIS}^2+2}{x_{SIS}\sqrt{x_{SIS}^2+4}}. \tag{66}$$

where x_{SIS}, $(\mu_{+}^{pl})_{SIS}$ and $(\mu_{-}^{pl})_{SIS}$ can be expressed as Atamurotov et al. (2022); Jiang et al.

(2024); Al-Badawi et al. (2024)

$$x_{SIS} = \frac{\beta}{(\theta_E^{pl})_{SIS}}, \tag{67}$$

$$(\mu_+^{pl})_{SIS} = \frac{1}{4}\left(\frac{x_{SIS}}{\sqrt{x_{SIS}^2+4}} + \frac{\sqrt{x_{SIS}^2+4}}{x_{SIS}} + 2\right), \tag{68}$$

$$(\mu_-^{pl})_{SIS} = \frac{1}{4}\left(\frac{x_{SIS}}{\sqrt{x_{SIS}^2+4}} + \frac{\sqrt{x_{SIS}^2+4}}{x_{SIS}} - 2\right), \tag{69}$$

We demonstrate the dependence of the total magnification on non-uniform plasma frequency for different values of the magnetic charge in Fig. 12. There is a decrease under the influence of the magnetic charge q. In addition, the values of the total magnification decrease with the increase of the non-uniform plasma frequency. To provide more information, we plot the dependence of the total magnification on x_0 for different values of the plasma frequency in Fig. 13. Notably, we find that the total magnification is reduced when influenced by non-uniform plasma, as opposed to the case with uniform plasma.

5. Parameter Estimation for MCBH Using EHT Data

To estimate the MCBH mass and magnetic charge parameters, we employed a Markov Chain Monte Carlo (MCMC) approach using the Python-based `emcee` library. The MCMC approach allows for the exploration of the posterior distribution of the parameters by sampling from the likelihood function.

The likelihood function was defined based on the observed shadow size from EHT observations of M87* and SgrA*. The shadow size is related to the photon orbit radius, which was computed by solving the radial geodesic equation for null geodesics. The photon orbit radius $r_{\rm ph}$ was obtained by numerically solving the equation:

$$\frac{df}{dr} - \frac{2}{r}f(r) = 0, \tag{70}$$

where $f(r)$ includes the exponential magnetic charge term. The shadow size was then computed using the relation:

$$R_{\rm sh} = r_{\rm ph}\sqrt{\frac{1}{f(r_{\rm ph})}}. \tag{71}$$

The predicted shadow size $\theta_{\rm sh}$ was scaled to microarcseconds using the relation:

$$\theta_{\rm sh} = R_{\rm sh} \times \frac{2M \times 4.847 \times 10^{-6}}{D}, \tag{72}$$

where D is the distance to the BH (16.8 Mpc for M87* and 0.0083 Mpc for SgrA*). The

log-likelihood function was defined as:

$$\log \mathcal{L}(M, q) = -\frac{1}{2} \sum_i \frac{(\theta_{\text{sh, predicted}} - \theta_{\text{sh, observed}})^2}{\sigma_i^2}, \tag{73}$$

where $\theta_{\text{sh, observed}}$ is the EHT shadow size and σ_i is the corresponding uncertainty.

The posterior probability was obtained using Bayes' theorem:

$$P(M, q|D) \propto \mathcal{L}(D|M, q) \cdot \pi(M, q), \tag{74}$$

where $\pi(M, q)$ is the prior distribution. We assumed uniform priors for the MCBH mass and magnetic charge within physically meaningful bounds:

$$5.5 \times 10^9 M_\odot < M_{MCBH} < 7.5 \times 10^9 M_\odot, \quad 0 \leq q_{\text{MCBH}} < 3.0 \times 10^9 M_\odot \quad \text{(for M87*)}, \tag{75}$$

$$3.0 \times 10^6 M_\odot < M_{MCBH} < 6.0 \times 10^6 M_\odot, \quad 0 \leq q_{\text{MCBH}} < 2.0 \times 10^6 M_\odot \quad \text{(for SgrA*)}. \tag{76}$$

We used 64 walkers and 50,000 MCMC steps for both M87* and SgrA*. The first 1,000 steps were discarded as burn-in, and the chains were thinned by a factor of 30 to reduce autocorrelation.

The posterior distribution of MCBH (using M87* data) was sampled efficiently, producing well-defined confidence contours in the parameter space of MCBH mass and magnetic charge. The best-fit values obtained from the MCMC sampling for MCBH are:

$$M_{\text{MCBH}} = 6.70^{+0.19}_{-0.19} \times 10^9 M_\odot, \tag{77}$$

$$q_{\text{MCBH}} = 0.63^{+0.68}_{-0.44} \times 10^9 M_\odot. \tag{78}$$

The posterior distribution for MCBH (using M87* data) is shown in Fig. 14, which illustrates a tight correlation between the mass and the magnetic charge parameter, indicating that the shadow size data from EHT places strong constraints on both parameters. The obtained mass value is consistent (i.e., within 1σ agreement) with the reported mass for M87* from EHT observations, which is $6.5^{+0.7}_{-0.7} \times 10^9 M_\odot$ Akiyama et al. (2019). The inferred magnetic charge value suggests the presence of a substantial magnetic component in the MCBH model for M87*. However, the relatively large asymmetric uncertainty—particularly the broader upper bound—indicates that the magnetic charge is not as tightly constrained as the mass parameter. This reflects a degree of parameter degeneracy in the shadow-based inference, although the posterior distribution still supports the viability of a non-zero magnetic charge in describing the observed shadow.

Similarly, the posterior distribution for MCBH (using SgrA* data) was well-sampled and showed a strong correlation between the MCBH mass and magnetic charge. The best-fit values for MCBH are:

$$M_{\text{MCBH}} = 4.08^{+0.19}_{-0.19} \times 10^6 M_\odot, \tag{79}$$

$$q_{\text{MCBH}} = 0.33^{+0.36}_{-0.23} \times 10^6 M_\odot. \tag{80}$$

The posterior distribution for the MCBH model using SgrA* data, as shown in Fig. 15, reveals a strong correlation between the mass and magnetic charge parameters. The estimated mass is in good agreement with the EHT-reported value of $4.0^{+1.1}_{-0.6} \times 10^6 M_\odot$ Collaboration (2022), lying within 1σ credible interval. The slight upward shift in the peak of the posterior distribution, relative to the EHT median, arises due to the effective modification of the gravitational potential

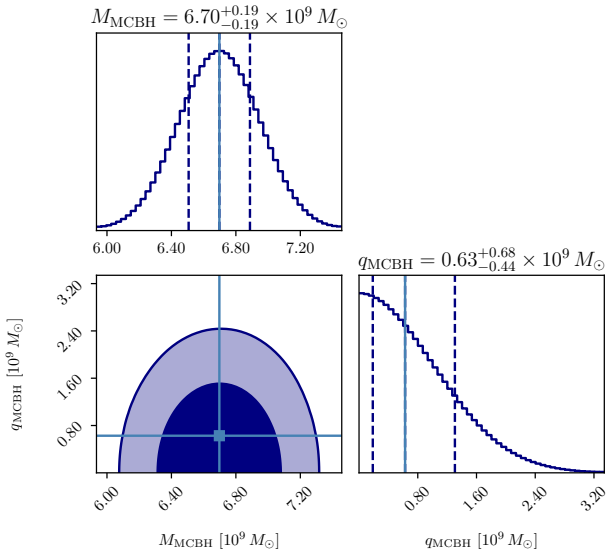

Figure 14: Plot showing the estimated MCBH mass and magnetic charge parameter using M87* EHT data.

in the MCBH spacetime. Specifically, the exponential magnetic charge term alters the spacetime curvature near the photon orbit, allowing the model to reproduce the observed shadow size with a marginally higher mass estimate. The inferred magnetic charge is notably smaller than the charge estimated for M87*, which aligns with expectations given the lower mass and possibly less magnetically dominated environment of SgrA*. Nonetheless, the presence of a non-zero magnetic charge suggests that even the spacetime surrounding SgrA* may be influenced by magnetic effects, potentially enhanced by its turbulent accretion dynamics. These findings reinforce the viability of the MCBH model and highlight the potential role of magnetic fields in shaping near-horizon BH geometries.

The consistent estimation of the MCBH mass and magnetic charge for both M87* and SgrA* reinforces the viability of the modified exponential metric model. The presence of a nonzero magnetic charge term indicates that magnetic fields may play a significant role in shaping the near-horizon spacetime geometry. For M87*, the estimated magnetic charge $q_{\rm MCBH} = (0.63^{+0.68}_{-0.44}) \times 10^9\, M_\odot$ is comparable to the mass scale, suggesting that the magnetic contribution is substantial and potentially close to the theoretical limit for horizonless configurations. In contrast, for SgrA*, the inferred magnetic charge $q_{\rm MCBH} = (0.33^{+0.36}_{-0.23}) \times 10^6\, M_\odot$ is relatively smaller, though still indicative of a non-negligible influence from magnetic effects—possibly amplified by the dynamic magnetohydrodynamic environment of the Galactic Center. Importantly, the mass estimates for both sources are consistent with the EHT results within the respective 1σ credible intervals. For example, the upper bound of the inferred mass for M87*, $6.89 \times 10^6\, M_\odot$, lies well within the EHT's reported 1σ range of $[5.8,\ 7.2] \times 10^9\, M_\odot$ Akiyama et al. (2019). This statistical agreement, despite the geometric differences from standard Kerr spacetime, reflects the robustness of the modified model and the effectiveness of MCMC sampling in constraining BH

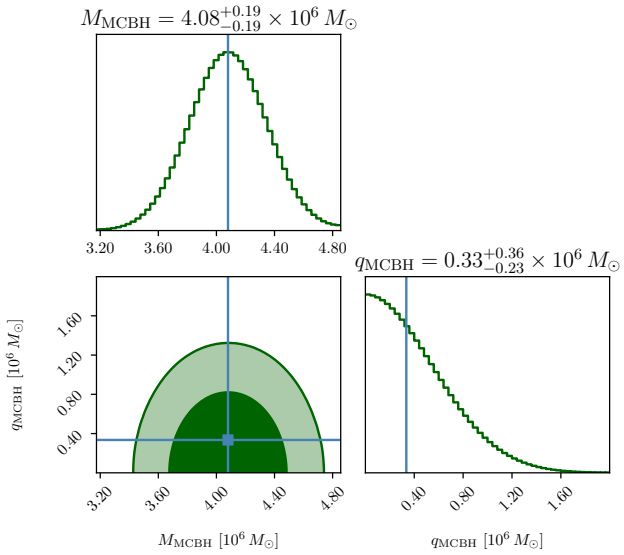

Figure 15: Plot showing the estimated MCBH mass and magnetic charge parameter using SgrA* EHT data.

Table 1: Estimated Parameters for MCBH

BH	Mass Estimate (M_{MCBH})	Magnetic Charge Estimate (q_{MCBH})
M87*	$(6.70^{+0.19}_{-0.19}) \times 10^9 M_\odot$	$0.63^{+0.68}_{-0.44} \times 10^9 M_\odot$
SgrA*	$(4.08^{+0.19}_{-0.19}) \times 10^6 M_\odot$	$0.33^{+0.36}_{-0.23} \times 10^6 M_\odot$

parameters. Overall, the results support the interpretation that magnetic fields—encoded via a phenomenological exponential charge term—could play a fundamental role in the geometry and observable features of BHs.

6. Conclusions

In this paper, we investigated the geometry of MCBHs and derived theoretical bounds on the magnetic charge parameter q Fig.1. We analyzed the optical properties of MCBHs, including BH shadows, gravitational lensing, and magnification effects in the presence of different plasma environments. Additionally, we performed Bayesian parameter estimation using observational data from the EHT to constrain the mass and magnetic charge of M87* and SgrA*. Our analysis demonstrates that the presence of a magnetic charge significantly modifies the spacetime geometry and observational signatures of BHs.

We first studied the theoretical shadow structure of MCBHs, showing that as the magnetic charge q increases, the shadow radius decreases (see Fig. 4). The presence of a plasma medium

further reduces the shadow size, with higher plasma density shifting the shadow to a smaller radius. The results indicate that both the magnetic charge and plasma environment strongly influence BH imaging. We also analyzed gravitational lensing around MCBHs in uniform and non-uniform plasma environments, finding that increasing q leads to a decrease in the deflection angle, suggesting that magnetization weakens gravitational lensing effects. The comparison of uniform and non-uniform plasma models revealed that uniform plasma produces a larger deflection angle. Furthermore, our study of total magnification in gravitational lensing scenarios demonstrated that the magnification decreases with increasing q, with images formed in uniform plasma exhibiting stronger magnification than those in non-uniform plasma.

To test the viability of the exponential magnetic charge in the MCBH metric, we employed MCMC sampling to constrain the mass and charge parameters using EHT observations of M87* and SgrA*. For M87*, the posterior distribution exhibits a pronounced correlation between mass and magnetic charge, underscoring that shadow size data imposes strong joint constraints. The estimated mass, $M_{\rm MCBH} = (6.70^{+0.19}_{-0.19}) \times 10^9\, M_\odot$, is approximately 3% higher than the EHT-reported central value of $6.5 \times 10^9\, M_\odot$, but remains within the 68% credible interval (i.e. within 1σ agreement), which spans from 5.8 to $7.2 \times 10^9\, M_\odot$ Akiyama et al. (2019). The MCBH value thus lies just inside this interval, and from a Bayesian perspective, this constitutes statistical agreement.

The magnetic charge estimate, $q_{\rm MCBH} = (0.63^{+0.68}_{-0.44}) \times 10^9\, M_\odot$, suggests that M87* may harbor a non-negligible magnetic component that subtly influences the observed photon ring structure. For SgrA*, the inferred posterior similarly reflects a strong mass-charge correlation, yielding an estimated mass $M_{\rm MCBH} = (4.08^{+0.19}_{-0.19}) \times 10^6\, M_\odot$, which is slightly higher than the EHT-reported value of $4.0 \times 10^6\, M_\odot$ Collaboration (2022), yet still consistent (close) with the 1σ agreement interval. The magnetic charge, $q_{\rm MCBH} = (0.33^{+0.36}_{-0.23}) \times 10^6\, M_\odot$, implies that the spacetime near SgrA* may also be influenced by magnetic effects, potentially amplified by its highly dynamic magnetohydrodynamic environment. The overall consistency between model-constrained and observed mass values for both sources affirms the robustness of the MCBH framework and supports the broader hypothesis that magnetic fields could play a significant role in modifying BH spacetimes.

Overall, our results demonstrate that the exponential magnetic charge metric provides a physically consistent explanation for the observed shadows of M87* and SgrA*, reinforcing the idea that strong magnetic fields influence the BH spacetime and observational features. Although the uncertainties in q are relatively large, the posterior distribution remains informative, indicating that the model captures key features of the observational data and provides a viable framework for exploring MCBHs. Future work could extend this analysis by incorporating higher-order corrections to the magnetic charge, investigating potential polarization effects in EHT observations, and testing the model against future BH imaging data from next-generation observatories such as the ngEHT and LISA. The findings presented in this study suggest that the presence of a magnetic charge is not only a theoretical possibility but may have observable consequences in strong gravitational lensing, shadow formation, and astrophysical plasma interactions, offering new insights into the fundamental nature of BHs.

acknowledgements

PS expresses gratitude to the Vellore Institute of Technology for financial support through its Seed Grant (No. SG20230079, Year 2023). Additionally, he acknowledges the support of

the Anusandhan National Research Foundation (ANRF) through the Science and Engineering Research Board (SERB) Core Research Grant (Grant No. CRG/2023/008980). SS is supported by the National Natural Science Foundation of China under Grant No. W2433018.

References

Abbott, B.P., et al. (LIGO Scientific, Virgo), 2016. Observation of Gravitational Waves from a Binary Black Hole Merger. Phys. Rev. Lett. 116, 061102. doi:10.1103/PhysRevLett.116.061102, arXiv:1602.03837.

Abdujabbarov, A., Amir, M., Ahmedov, B., Ghosh, S.G., 2016. Shadow of rotating regular black holes. Phys. Rev. D 93, 104004. doi:10.1103/PhysRevD.93.104004, arXiv:1604.03809.

Akiyama, K., et al. (Event Horizon Telescope Collaboration), 2019a. First M87 Event Horizon Telescope Results. I. The Shadow of the Supermassive Black Hole. Astrophys. J. 875, L1. doi:10.3847/2041-8213/ab0ec7, arXiv:1906.11238.

Akiyama, K., et al. (Event Horizon Telescope Collaboration), 2019b. First M87 Event Horizon Telescope Results. VI. The Shadow and Mass of the Central Black Hole. Astrophys. J. 875, L6. doi:10.3847/2041-8213/ab1141, arXiv:1906.11243.

Akiyama, K., et al. (Event Horizon Telescope Collaboration), 2021. First M87 Event Horizon Telescope Results. VII. Polarization of the Ring. Astrophys. J. 910, L12. doi:10.3847/2041-8213/abe71d.

Akiyama, K., et al. (Event Horizon Telescope), 2019. First M87 Event Horizon Telescope Results. I. The Shadow of the Supermassive Black Hole. Astrophys. J. Lett. 875, L1. doi:10.3847/2041-8213/ab0ec7, arXiv:1906.11238.

Al-Badawi, A., Shaymatov, S., Alloqulov, M., Wang, A., 2024. A regular MOG black hole's impact on shadows and gravitational weak lensing in the presence of a quintessence field. Commun. Theor. Phys. 76, 085401. doi:10.1088/1572-9494/ad4c55, arXiv:2401.12723.

Ali, M.S., Ghosh, S.G., Maharaj, S.D., 2020. Effective thermodynamics and critical phenomena of rotating regular-de sitter black holes. Classical and Quantum Gravity 37, 185003. URL: https://dx.doi.org/10.1088/1361-6382/ab9c6c, doi:10.1088/1361-6382/ab9c6c.

Alloqulov, M., Atamurotov, F., Abdujabbarov, A., Ahmedov, B., 2023. Probing Hořava-Lifshitz gravity using particle and photon dynamics in the presence of plasma*. Chin. Phys. C 47, 075103. URL: https://dx.doi.org/10.1088/1674-1137/acd43c, doi:10.1088/1674-1137/acd43c.

Alloqulov, M., Atamurotov, F., Abdujabbarov, A., Ahmedov, B., Khamidov, V., 2024a. Shadow and weak gravitational lensing for Ellis-Bronnikov wormhole*. Chin. Phys. C 48, 025104. URL: https://dx.doi.org/10.1088/1674-1137/ad1677, doi:10.1088/1674-1137/ad1677.

Alloqulov, M., Shaymatov, S., Jawad, A., Zaripov, O., 2024b. Plasma impact on black hole shadows and gravitational weak lensing in the Einstein–Maxwell-scalar theory. Communications in Theoretical Physics 77, 015402. URL: https://dx.doi.org/10.1088/1572-9494/ad7831, doi:10.1088/1572-9494/ad7831.

Astropy Collaboration, 2013. Astropy: A community Python package for astronomy. Astron. Astrophys. 558, A33. doi:10.1051/0004-6361/201322068, arXiv:1307.6212.

Astropy Collaboration, 2018. The Astropy Project: Building an Open-science Project and Status of the v2.0 Core Package. Astron. J. 156, 123. doi:10.3847/1538-3881/aabc4f, arXiv:1801.02634.

Atamurotov, F., Alloqulov, M., Abdujabbarov, A., Ahmedov, B., 2022. Testing the Einstein-Æther gravity: particle dynamics and gravitational lensing. The European Physical Journal Plus 137, 634. URL: https://doi.org/10.1140/epjp/s13360-022-02846-w, doi:10.1140/epjp/s13360-022-02846-w.

Atamurotov, F., Shaymatov, S., Sheoran, P., Siwach, S., 2021. Charged black hole in 4D Einstein-Gauss-Bonnet gravity: particle motion, plasma effect on weak gravitational lensing and centre-of-mass energy. JCAP 2021, 045. doi:10.1088/1475-7516/2021/08/045, arXiv:2105.02214.

Ayon-Beato, E., Garcia, A., 1998. Regular black hole in general relativity coupled to nonlinear electrodynamics. Phys. Rev. Lett. 80, 5056–5059. doi:10.1103/PhysRevLett.80.5056, arXiv:gr-qc/9911046.

Ayon-Beato, E., Garcia, A., 2000. The Bardeen model as a nonlinear magnetic monopole. Phys. Lett. B 493, 149–152. doi:10.1016/S0370-2693(00)01125-4, arXiv:gr-qc/0009077.

Babar, G.Z., Atamurotov, F., Babar, A.Z., 2021. Gravitational lensing in 4-d einstein–gauss–bonnet gravity in the presence of plasma. Physics of the Dark Universe 32, 100798. URL: https://www.sciencedirect.com/science/article/pii/S2212686421000297, doi:https://doi.org/10.1016/j.dark.2021.100798.

Balart, L., Vagenas, E.C., 2014. Regular black hole metrics and the weak energy condition. Phys. Lett. B 730, 14–17. doi:10.1016/j.physletb.2014.01.024, arXiv:1401.2136.

Bambi, C., Freese, K., Vagnozzi, S., Visinelli, L., 2019. Testing the rotational nature of the supermassive object M87* from the circularity and size of its first image. Physical Review D 100. URL: http://dx.doi.org/10.1103/PhysRevD.100.044057, doi:10.1103/physrevd.100.044057.

Bardeen, J., 1968. Non-singular general relativistic gravitational collapse, in: Proceedings of the 5th International Conference on Gravitation and the Theory of Relativity, p. 87.

Bardeen, J.M., 1968. Non-singular general-relativistic gravitational collapse, in: Proceedings of International Conference GR5, Tbilisi, USSR. p. 174.

Bartelmann, M., Schneider, P., 2001. Weak gravitational lensing. Physics Reports 340, 291–472. URL: http://dx.doi.org/10.1016/S0370-1573(00)00082-X, doi:10.1016/s0370-1573(00)00082-x.

Bisnovatyi-Kogan, G.S., Tsupko, O.Y., 2009. Gravitational radiospectrometer. Gravitation and Cosmology 15, 20–27. URL: http://dx.doi.org/10.1134/S020228930901006X, doi:10.1134/s020228930901006x.

Bisnovatyi-Kogan, G.S., Tsupko, O.Y., 2010. Gravitational lensing in a non-uniform plasma. MNRAS 404, 1790–1800. URL: https://doi.org/10.1111/j.1365-2966.2010.16290.x, doi:10.1111/j.1365-2966.2010.16290.x.

Bisnovatyi-Kogan, G.S., Tsupko, O.Y., 2017. Gravitational Lensing in Presence of Plasma: Strong Lens Systems, Black Hole Lensing and Shadow. Universe 3, 57. doi:10.3390/universe3030057, arXiv:1905.06615.

Bozza, V., 2008. Comparison of approximate gravitational lens equations and a proposal for an improved new one. Phys. Rev. D 78, 103005. URL: https://link.aps.org/doi/10.1103/PhysRevD.78.103005, doi:10.1103/PhysRevD.78.103005.

Bozza, V., Capozziello, S., Iovane, G., Scarpetta, G., 2001. Strong field limit of black hole gravitational lensing. General Relativity and Gravitation 33, 1535–1548. URL: http://dx.doi.org/10.1023/A:1012292927358, doi:10.1023/a:1012292927358, arXiv:gr-qc/0102068.

Bronnikov, K.A., 2001. Regular magnetic black holes and monopoles from nonlinear electrodynamics. Phys. Rev. D 63, 044005. doi:10.1103/PhysRevD.63.044005, arXiv:gr-qc/0006014.

Collaboration, E.H.T., 2022. First Sagittarius A* Event Horizon Telescope Results. I. The Shadow of the Supermassive Black Hole in the Center of the Milky Way. Astrophys. J. Lett. 930, L12. doi:10.3847/2041-8213/ac6674.

Cunha, P.V.P., Herdeiro, C.A.R., Radu, E., Runarsson, H.F., 2017. Shadows of Kerr Black Holes with Scalar Hair. Phys. Rev. D 96, 104040. arXiv:1709.06118.

Dymnikova, I., 1992. Vacuum nonsingular black hole. Gen. Rel. Grav. 24, 235–242. doi:10.1007/BF00760226.

Eckart, A., Zensus, J.A., Bower, G., Schödel, R., García-Marín, M., Witzel, G., et al., 2017. The milky way's supermassive black hole: How good a case is it? Foundations of Physics 47, 553–624. URL: https://doi.org/10.1007/s10701-017-0079-2, doi:10.1007/s10701-017-0079-2.

Er, X., Mao, S., 2014. Testing black hole candidates with electromagnetic radiation. Mon. Not. R. Astron. Soc. 437, 2180–2186. arXiv:1310.5825.

Fan, Z.Y., Wang, X., 2016. Construction of Regular Black Holes in General Relativity. Phys. Rev. D 94, 124027. doi:10.1103/PhysRevD.94.124027, arXiv:1610.02636.

Foreman-Mackey, D., Hogg, D.W., Lang, D., Goodman, J., 2013. emcee: The MCMC Hammer. Publ. Astron. Soc. Pac. 125, 306. doi:10.1086/670067, arXiv:1202.3665.

Genzel, R., Eisenhauer, F., Gillessen, S., 2010. The Galactic Center massive black hole and nuclear star cluster. Rev. Mod. Phys. 82, 3121–3195. doi:10.1103/RevModPhys.82.3121, arXiv:1006.0064.

Ghosh, S.G., Walia, R.K., 2021. Rotating black holes in general relativity coupled to nonlinear electrodynamics. Annals of Physics 434, 168619. URL: http://dx.doi.org/10.1016/j.aop.2021.168619, doi:10.1016/j.aop.2021.168619.

Hawking, S.W., Penrose, R., 1970. The Singularities of gravitational collapse and cosmology. Proc. Roy. Soc. Lond. A 314, 529–548. doi:10.1098/rspa.1970.0021.

Hendi, S.H., Panahiyan, S., Eslam Panah, B., Momennia, M., 2017. Critical behavior of Born-Infeld AdS black holes in higher dimensions. Annals Phys. 383, 257–267. arXiv:1608.03148.

Hioki, A., Maeda, K.i., 2009. Measurement of the Kerr Spin Parameter by Observation of a Compact Object's Shadow. Phys. Rev. D 80, 024042. arXiv:0904.3575.

Jafarzade, K., Shaymatov, S., Jamil, M., 2025. Shadows and optical appearances of black holes in R^2 gravity. Astroparticle Physics 168, 103100. URL: https://www.sciencedirect.com/science/article/pii/S0927650525000234, doi:https://doi.org/10.1016/j.astropartphys.2025.103100, arXiv:2502.14980.

Jiang, H., Alloqulov, M., Wu, Q., Shaymatov, S., Zhu, T., 2024. Periodic orbits and plasma effects on gravitational weak lensing by self-dual black hole in loop quantum gravity. Phys. Dark Universe 46, 101627. doi:10.1016/j.dark.2024.101627.

Konoplya, R.A., 2019. Shadow of a black hole surrounded by dark matter. Physics Letters B 795. doi:10.1016/j.physletb.2019.05.043.

Kubiznak, D., Mann, R.B., 2012. P-V criticality of charged AdS black holes. JHEP 07, 033. arXiv:1205.0559.

Kumar, R., Kumar, A., Ghosh, S.G., 2020. Testing rotating regular metrics as candidates for astrophysical black holes. Mon. Not. R. Astron. Soc. 497, 3845–3856. doi:10.1093/mnras/staa2104, arXiv:2006.09869.

Mustafa, G., Atamurotov, F., Hussain, I., Shaymatov, S., Övgün, A., 2022. Shadows and gravitational weak lensing by the Schwarzschild black hole in the string cloud background with quintessential field. Chin. Phys. C 46, 125107.

doi:10.1088/1674-1137/ac917f, arXiv:2207.07608.

Narzilloev, B., Rayimbaev, J., Shaymatov, S., Abdujabbarov, A., Ahmedov, B., Bambi, C., 2020. Dynamics of test particles around a Bardeen black hole surrounded by perfect fluid dark matter. Phys. Rev. D 102, 104062. doi:10.1103/PhysRevD.102.104062, arXiv:2011.06148.

Neves, J.C.S., Saa, A., 2014. Regular rotating black holes and the weak energy condition. Phys. Lett. B 734, 44–48. doi:10.1016/j.physletb.2014.05.026, arXiv:1402.2694.

Parthasarathy, S., Wagh, S.M., Dhurandhar, S.V., Dadhich, N., 1986. A New Look at the Penrose Process. Mon. Not. R. Astron. Soc. 218, 411–419.

Penrose, R., 1969. Gravitational Collapse: The Role of General Relativity. Nuovo Cimento 1, 252–276. [Reprinted in Gen. Rel. Grav. 34, 1141 (2002)].

Perlick, V., Tsupko, O.Y., Bisnovatyi-Kogan, G.S., 2015. Influence of a plasma on the shadow of a spherically symmetric black hole. Phys. Rev. D. 92, 104031. doi:10.1103/PhysRevD.92.104031, arXiv:1507.04217.

Perlick, V., Tsupko, O.Y., Bisnovatyi-Kogan, G.S., 2018. Black hole shadow in an expanding universe with a cosmological constant. Phys. Rev. D 97, 104062. doi:10.1103/PhysRevD.97.104062, arXiv:1804.04898.

Perlmutter, S., et al. (Supernova Cosmology Project), 1999. Measurements of Ω and Λ from 42 High Redshift Supernovae. Astrophys. J. 517, 565–586. doi:10.1086/307221, arXiv:astro-ph/9812133.

Psaltis, D., et al. (Event Horizon Telescope), 2020. Gravitational Test Beyond the First Post-Newtonian Order with the Shadow of the M87 Black Hole. Phys. Rev. Lett. 125, 141104. doi:10.1103/PhysRevLett.125.141104, arXiv:2010.01055.

Rayimbaev, J., Kurbonov, N., Abdujabbarov, A., Han, W.B., 2022. Dynamics of test particles around magnetically charged regular black holes. International Journal of Modern Physics D 31, 2250032–266. doi:10.1142/S0218271822500328.

Riess, A.G., et al. (Supernova Search Team), 1998. Observational evidence from supernovae for an accelerating universe and a cosmological constant. Astron. J. 116, 1009–1038. doi:10.1086/300499, arXiv:astro-ph/9805201.

Rogers, A., 2015a. Frequency-dependent effects of gravitational lensing within plasma. Mon. Not. R. Astron. Soc. 451, 17–25. doi:10.1093/mnras/stv917, arXiv:1505.06790.

Rogers, A., 2015b. 'Frequency-dependent effects of gravitational lensing within plasma'. Mon. Not. R. Astron. Soc. 451, 17. doi:10.1093/mnras/stv903.

Schneider, P., Ehlers, J., Falco, E.E., 1992. Gravitational lensing. Springer- Verlag, Berlin.

Shaymatov, S., Ahmedov, B., De Laurentis, M., Jamil, M., Wu, Q., Wang, A., Azreg-Aïnou, M., 2023. On the Parameters of the Spherically Symmetric Parameterized Rezzolla-Zhidenko Spacetime through Solar System Tests, the Orbit of the S2 Star about Sgr A*, and Quasiperiodic Oscillations. Astrophys. J. 959, 6. doi:10.3847/1538-4357/acfcba, arXiv:2307.10804.

Shaymatov, S., Sheoran, P., Becerril, R., Nucamendi, U., Ahmedov, B., 2022. Efficiency of Penrose process in spacetime of axially symmetric magnetized Reissner-Nordström black hole. Phys. Rev. D 106, 024039. doi:10.1103/PhysRevD.106.024039, arXiv:2204.02026.

Synge, J.L. (Ed.), 1960. Relativity: The General theory. North-Holland, Amsterdam,.

Synge, J.L., 1966. The Escape of Photons from Gravitationally Intense Stars. Mon. Not. R. Astron. Soc. 131, 463–466.

Toshmatov, B., Ahmedov, B., Abdujabbarov, A., Stuchlík, Z., 2014. Rotating regular black hole solution. Phys. Rev. D 89, 104017. URL: https://link.aps.org/doi/10.1103/PhysRevD.89.104017, doi:10.1103/PhysRevD.89.104017, arXiv:1404.6443.

Tsupko, O.Y., Bisnovatyi-Kogan, G.S., 2009. 'Relativistic Rings Due to Schwarzschild Gravitational Lensing'. Gravit. Cosmol. 15, 184. doi:10.1134/S0202289309020182.

Will, C.M., 2014. The Confrontation between General Relativity and Experiment. Living Rev. Rel. 17, 4. doi:10.12942/lrr-2014-4, arXiv:1403.7377.

Xamidov, T., Shaymatov, S., Sheoran, P., Ahmedov, B., 2024. Astrophysical insights into magnetic Penrose process around parameterized Konoplya–Rezzolla–Zhidenko black hole. Eur. Phys. J. C 84, 1300. doi:10.1140/epjc/s10052-024-13658-w, arXiv:2407.19800.

Xamidov, T., Sheoran, P., Shaymatov, S., Zhu, T., 2025. Energy extraction from Loop Quantum Black Holes: the role of magnetic Penrose process and quantum gravity effects with astrophysical insights. J. Cosmol. Astropart. Phys. 2025, 053. doi:10.1088/1475-7516/2025/03/053, arXiv:2412.03885.